

Measurements of the branching fractions of $\Xi_c^0 \rightarrow \Xi^0 \pi^0$, $\Xi_c^0 \rightarrow \Xi^0 \eta$, and $\Xi_c^0 \rightarrow \Xi^0 \eta'$ and asymmetry parameter of $\Xi_c^0 \rightarrow \Xi^0 \pi^0$

The Belle and Belle II Collaborations

I. Adachi , L. Aggarwal , H. Aihara , N. Akopov , A. Aloisio , N. Althubiti , N. Anh Ky , D. M. Asner , H. Atmacan , T. Aushev , V. Aushev , M. Aversano , R. Ayad , V. Babu , H. Bae , S. Bahinipati , P. Bambade , Sw. Banerjee , M. Barrett , J. Baudot , A. Baur , A. Beaubien , F. Becherer , J. Becker , J. V. Bennett , F. U. Bernlochner , V. Bertacchi , M. Bertemes , E. Bertholet , M. Bessner , S. Bettarini , B. Bhuyan , F. Bianchi , L. Bierwirth , T. Bilka , D. Biswas , A. Bobrov , D. Bodrov , J. Borah , A. Boschetti , A. Bozek , M. Bračko , P. Branchini , T. E. Browder , A. Budano , S. Bussino , Q. Campagna , M. Campajola , L. Cao , G. Casarosa , C. Cecchi , J. Cerasoli , M.-C. Chang , P. Chang , P. Cheema , C. Chen , B. G. Cheon , K. Chilikin , K. Chirapatpimol , H.-E. Cho , K. Cho , S.-J. Cho , S.-K. Choi , S. Choudhury , L. Corona , J. X. Cui , F. Dattola , E. De La Cruz-Burelo , S. A. De La Motte , G. De Nardo , G. De Pietro , R. de Sangro , M. Destefanis , S. Dey , R. Dhamija , A. Di Canto , F. Di Capua , J. Dingfelder , Z. Doležal , I. Domínguez Jiménez , T. V. Dong , M. Dorigo , K. Dort , D. Dossett , S. Dubey , K. Dugic , G. Dujany , P. Ecker , M. Eliachevitch , D. Epifanov , P. Feichtinger , T. Ferber , T. Fillinger , C. Finck , A. Fodor , F. Forti , A. Frey , B. G. Fulsom , A. Gabrielli , G. Gaudino , V. Gaur , A. Gaz , A. Gellrich , G. Ghevondyan , D. Ghosh , H. Ghumaryan , G. Giakoustidis , R. Giordano , A. Giri , A. Glazov , B. Gobbo , R. Godang , O. Gogota , P. Goldenzweig , W. Gradl , E. Graziani , D. Greenwald , Z. Gruberová , T. Gu , K. Gudkova , I. Haide , S. Halder , Y. Han , T. Hara , C. Harris , K. Hayasaka , H. Hayashii , S. Hazra , C. Hearty , M. T. Hedges , A. Heidelberg , I. Heredia de la Cruz , T. Higuchi , M. Hoek , M. Hohmann , P. Horak , C.-L. Hsu , T. Humair , K. Inami , N. Ipsita , A. Ishikawa , R. Itoh , M. Iwasaki , W. W. Jacobs , E.-J. Jang , S. Jia , Y. Jin , A. Johnson , K. K. Joo , H. Junkerkalefeld , M. Kaleta , J. Kandra , K. H. Kang , S. Kang , G. Karyan , F. Keil , C. Kiesling , C.-H. Kim , D. Y. Kim , K.-H. Kim , Y.-K. Kim , H. Kindo , K. Kinoshita , P. Kodyš , T. Koga , S. Kohani , K. Kojima , A. Korobov

S. Korpar , E. Kovalenko , R. Kowalewski , P. Križan , P. Krokovny , T. Kuhr ,
Y. Kulii , R. Kumar , K. Kumara , T. Kunigo , A. Kuzmin , Y.-J. Kwon ,
S. Lacaprara , K. Lalwani , T. Lam , J. S. Lange , M. Laurenza ,
R. Leboucher , M. J. Lee , C. Lemettais , P. Leo , D. Levit , P. M. Lewis ,
L. K. Li , S. X. Li , Y. Li , Y. B. Li , J. Libby , Z. Liptak , M. H. Liu ,
Q. Y. Liu , Z. Q. Liu , D. Liventsev , S. Longo , T. Lueck , C. Lyu , Y. Ma ,
M. Maggiora , S. P. Maharana , R. Maiti , S. Maity , G. Mancinelli ,
R. Manfredi , E. Manoni , M. Mantovano , D. Marcantonio , S. Marcello ,
C. Marinas , C. Martellini , A. Martens , A. Martini , T. Martinov ,
L. Massaccesi , M. Masuda , D. Matvienko , S. K. Maurya , J. A. McKenna ,
R. Mehta , F. Meier , M. Merola , C. Miller , M. Mirra , S. Mitra ,
K. Miyabayashi , G. B. Mohanty , S. Moneta , H.-G. Moser , M. Mrvar ,
I. Nakamura , M. Nakao , Y. Nakazawa , M. Naruki , Z. Natkaniec ,
A. Natochii , M. Nayak , G. Nazaryan , M. Neu , M. Niiyama , S. Nishida ,
S. Ogawa , Y. Onishchuk , H. Ono , G. Pakhlova , S. Pardi , K. Parham ,
H. Park , J. Park , S.-H. Park , A. Passeri , S. Patra , S. Paul , T. K. Pedlar ,
R. Peschke , R. Pestotnik , M. Piccolo , L. E. Piilonen , G. Pinna Angioni ,
P. L. M. Podesta-Lerma , T. Podobnik , S. Pokharel , C. Praz , S. Prell ,
E. Prencipe , M. T. Prim , H. Purwar , P. Rados , G. Raeuber , S. Raiz ,
N. Rauls , M. Reif , S. Reiter , M. Remnev , L. Reuter , I. Ripp-Baudot ,
G. Rizzo , M. Roehrken , J. M. Roney , A. Rostomyan , N. Rout , S. Sandilya ,
L. Santelj , Y. Sato , V. Savinov , B. Scavino , S. Schneider , M. Schnepf ,
C. Schwanda , Y. Seino , A. Selce , K. Senyo , J. Serrano , M. E. Sevier ,
C. Sfienti , W. Shan , C. Sharma , C. P. Shen , X. D. Shi , T. Shillington ,
T. Shimasaki , J.-G. Shiu , D. Shtol , A. Sibidanov , F. Simon , J. B. Singh ,
J. Skorupa , R. J. Sobie , M. Sobotzik , A. Soffer , E. Solovieva , W. Song ,
S. Spataro , B. Spruck , M. Starič , P. Stavroulakis , S. Stefkova , R. Stroili ,
M. Sumihama , K. Sumisawa , N. Suwonjandee , H. Svidras , M. Takahashi ,
M. Takizawa , S. Tanaka , K. Tanida , F. Tenchini , A. Thaller , O. Tittel ,
R. Tiwary , D. Tonelli , E. Torassa , K. Trabelsi , I. Ueda , T. Uglov ,
K. Unger , Y. Unno , K. Uno , S. Uno , S. E. Vahsen , R. van Tonder ,
K. E. Varvell , M. Veronesi , A. Vinokurova , V. S. Vismaya , L. Vitale ,
V. Vobbiliseti , R. Volpe , A. Vossen , M. Wakai , S. Wallner , E. Wang ,
M.-Z. Wang , Z. Wang , A. Warburton , S. Watanuki , C. Wessel , E. Won ,
X. P. Xu , B. D. Yabsley , S. Yamada , W. Yan , S. B. Yang , J. Yelton ,
J. H. Yin , Y. M. Yook , K. Yoshihara , C. Z. Yuan , L. Zani , F. Zeng ,
B. Zhang , V. Zhilich , J. S. Zhou , Q. D. Zhou , V. I. Zhukova , R. Žlebčik 

ABSTRACT: We present a study of $\Xi_c^0 \rightarrow \Xi^0 \pi^0$, $\Xi_c^0 \rightarrow \Xi^0 \eta$, and $\Xi_c^0 \rightarrow \Xi^0 \eta'$ decays using the Belle and Belle II data samples, which have integrated luminosities of 980 fb^{-1} and 426 fb^{-1} , respectively. We measure the following relative branching fractions

$$\mathcal{B}(\Xi_c^0 \rightarrow \Xi^0 \pi^0)/\mathcal{B}(\Xi_c^0 \rightarrow \Xi^- \pi^+) = 0.48 \pm 0.02(\text{stat}) \pm 0.03(\text{syst}),$$

$$\mathcal{B}(\Xi_c^0 \rightarrow \Xi^0 \eta)/\mathcal{B}(\Xi_c^0 \rightarrow \Xi^- \pi^+) = 0.11 \pm 0.01(\text{stat}) \pm 0.01(\text{syst}),$$

$$\mathcal{B}(\Xi_c^0 \rightarrow \Xi^0 \eta')/\mathcal{B}(\Xi_c^0 \rightarrow \Xi^- \pi^+) = 0.08 \pm 0.02(\text{stat}) \pm 0.01(\text{syst})$$

for the first time, where the uncertainties are statistical (stat) and systematic (syst). By multiplying by the branching fraction of the normalization mode, $\mathcal{B}(\Xi_c^0 \rightarrow \Xi^- \pi^+)$, we obtain the following absolute branching fraction results $(6.9 \pm 0.3(\text{stat}) \pm 0.5(\text{syst}) \pm 1.3(\text{norm})) \times 10^{-3}$, $(1.6 \pm 0.2(\text{stat}) \pm 0.2(\text{syst}) \pm 0.3(\text{norm})) \times 10^{-3}$, and $(1.2 \pm 0.3(\text{stat}) \pm 0.1(\text{syst}) \pm 0.2(\text{norm})) \times 10^{-3}$, for Ξ_c^0 decays to $\Xi^0 \pi^0$, $\Xi^0 \eta$, and $\Xi^0 \eta'$ final states, respectively. The third errors are from the uncertainty on $\mathcal{B}(\Xi_c^0 \rightarrow \Xi^- \pi^+)$. The asymmetry parameter for $\Xi_c^0 \rightarrow \Xi^0 \pi^0$ is measured to be $\alpha(\Xi_c^0 \rightarrow \Xi^0 \pi^0) = -0.90 \pm 0.15(\text{stat}) \pm 0.23(\text{syst})$.

KEYWORDS: e^+e^- Experiments, charmed baryon, Cabibbo-favored decay

Contents

1	Introduction	1
2	Belle and Belle II detectors	3
3	Data sample	4
4	Selection criteria	4
5	Branching fractions for $\Xi_c^0 \rightarrow \Xi^0 \pi^0$, $\Xi_c^0 \rightarrow \Xi^0 \eta$, and $\Xi_c^0 \rightarrow \Xi^0 \eta'$	6
6	Asymmetry parameter of $\Xi_c^0 \rightarrow \Xi^0 \pi^0$	10
7	Systematic uncertainties	12
7.1	Branching fraction ratios	12
7.2	Asymmetry parameter	13
8	Summary and discussion	14
A	$M(\Xi^0 \pi^0)$ spectra in $\cos \theta_{\Xi^0}$ bins	19

1 Introduction

Charmed baryons provide an interesting dynamical system to study the interplay of strong and weak interactions. Recently, there have been several impactful measurements for the Ξ_c^0 baryon. In particular, the absolute branching fractions of several Ξ_c^0 decay modes, especially the normalization mode $\Xi_c^0 \rightarrow \Xi^- \pi^+$, have been measured [1], allowing for the determination of branching fractions for other channels using ratios of branching fractions. In addition, the Belle experiment has recently measured branching fractions and decay asymmetry parameters for several Cabibbo-favored (CF) decays, including the two-body $\Xi_c^0 \rightarrow B V$ decays $\Xi_c^0 \rightarrow \Lambda \bar{K}^{*0}$, $\Sigma^0 \bar{K}^{*0}$, and $\Sigma^+ K^{*-}$ [2] as well as the branching fractions for the two-body $\Xi_c^0 \rightarrow B P$ decays $\Xi_c^0 \rightarrow \Lambda K_S^0$, $\Sigma^0 K_S^0$, and $\Sigma^+ K^-$ [3], where B , V , and P represent light baryons, vector mesons, and pseudoscalar mesons, respectively. Additional measurements of Ξ_c^0 branching fractions and decay asymmetry parameters may allow for a more complete description of the dynamics of the strong and weak interactions in charmed baryon decays.

In hadronic weak-interaction decays of charmed baryons, nonfactorizable amplitudes arising from internal W -emission and W -exchange quark-level processes play an essential role and lead to difficulties for theoretical predictions [4]. Figure 1 shows the Feynman diagrams for the internal W -emission and W -exchange amplitudes in CF $\Xi_c^0 \rightarrow \Xi^0 h^0$ decays,

to which only the nonfactorizable amplitudes contribute [4]. In the following, h^0 refers to π^0 , η , or η' mesons. Various approaches have been developed to describe the nonfactorizable effects, including the covariant confined quark model [5, 6], the pole model [7–10], and current algebra (CA) [8–11], and $SU(3)_F$ flavor symmetry [12–20] based treatments. Theoretical predictions for the branching fractions of $\Xi_c^0 \rightarrow \Xi^0 h^0$ decays based on these approaches are listed in table 1. Measurements of the branching fractions for $\Xi_c^0 \rightarrow \Xi^0 h^0$ decays will help to clarify the theoretical picture.

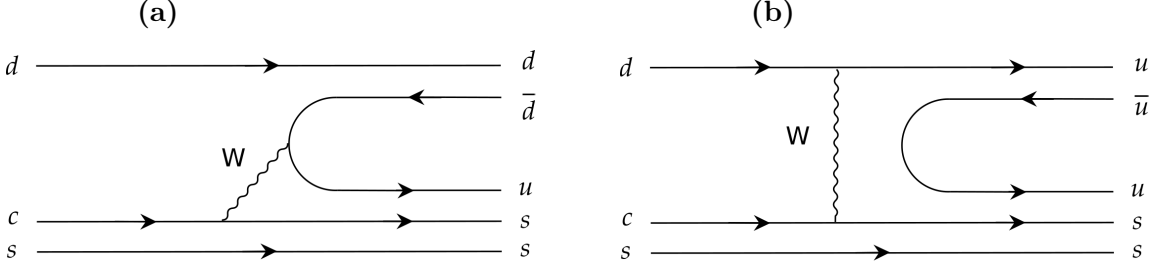


Figure 1. Feynman diagrams for (a) internal W -emission and (b) W -exchange in $\Xi_c^0 \rightarrow \Xi^0 h^0$ decays [4].

Table 1. Theoretical predictions for the branching fractions and decay asymmetry parameters for $\Xi_c^0 \rightarrow \Xi^0 h^0$ decays. Branching fractions are given in units of 10^{-3} .

Reference	Model	$\mathcal{B}(\Xi_c^0 \rightarrow \Xi^0 \pi^0)$	$\mathcal{B}(\Xi_c^0 \rightarrow \Xi^0 \eta)$	$\mathcal{B}(\Xi_c^0 \rightarrow \Xi^0 \eta')$	$\alpha(\Xi_c^0 \rightarrow \Xi^0 \pi^0)$
Körner, Krämer [5]	Quark	0.5	3.2	11.6	0.92
Ivanov <i>et al.</i> [6]	Quark	0.5	3.7	4.1	0.94
Xu, Kamal [7]	Pole	7.7	-	-	0.92
Cheng, Tseng [8]	Pole	3.8	-	-	-0.78
Żenczykowski [9]	Pole	6.9	1.0	9.0	0.21
Zou <i>et al.</i> [10]	Pole	18.2	26.7	-	-0.77
Sharma, Verma [11]	CA	-	-	-	-0.8
Cheng, Tseng [8]	CA	17.1	-	-	0.54
Geng <i>et al.</i> [12]	$SU(3)_F$	4.3 ± 0.9	$1.7^{+1.0}_{-1.7}$	$8.6^{+11.0}_{-6.3}$	-
Geng <i>et al.</i> [13]	$SU(3)_F$	7.6 ± 1.0	10.3 ± 2.0	9.1 ± 4.1	$-1.00^{+0.07}_{-0.00}$
Zhao <i>et al.</i> [14]	$SU(3)_F$	4.7 ± 0.9	8.3 ± 2.3	7.2 ± 1.9	-
Huang <i>et al.</i> [15]	$SU(3)_F$	2.56 ± 0.93	-	-	-0.23 ± 0.60
Hsiao <i>et al.</i> [16]	$SU(3)_F$	6.0 ± 1.2	$4.2^{+1.6}_{-1.3}$	-	-
Hsiao <i>et al.</i> [16]	$SU(3)_F$ -breaking	3.6 ± 1.2	7.3 ± 3.2	-	-
Zhong <i>et al.</i> [17]	$SU(3)_F$	$1.13^{+0.59}_{-0.49}$	1.56 ± 1.92	$0.683^{+3.272}_{-3.268}$	$0.50^{+0.37}_{-0.35}$
Zhong <i>et al.</i> [17]	$SU(3)_F$ -breaking	$7.74^{+2.52}_{-2.32}$	$2.43^{+2.79}_{-2.90}$	$1.63^{+5.09}_{-5.14}$	$-0.29^{+0.20}_{-0.17}$
Xing <i>et al.</i> [18]	$SU(3)_F$	1.30 ± 0.51	-	-	-0.28 ± 0.18
Geng <i>et al.</i> [19]	$SU(3)_F$	7.10 ± 0.41	2.94 ± 0.97	5.66 ± 0.93	-0.49 ± 0.09
Zhong <i>et al.</i> [20]	Diagrammatic- $SU(3)_F$	7.45 ± 0.64	2.87 ± 0.66	5.31 ± 1.33	-0.51 ± 0.08
Zhong <i>et al.</i> [20]	Irreducible- $SU(3)_F$	7.72 ± 0.65	2.28 ± 0.53	5.66 ± 1.62	-0.51 ± 0.09

In addition to the branching fraction measurement, parity violation can also be studied. In weak-interaction decays, the interference between the parity-violating and parity-conserving amplitudes leads to an asymmetry in the angular decay distribution, which can be quantified by the parameter α . In $\Xi_c^0 \rightarrow \Xi^0 h^0$ decays, α can be extracted by fitting to

the Ξ_c^0 decay angular distribution, using the differential decay rate function,

$$\frac{dN}{d\cos\theta_{\Xi^0}} \propto 1 + \alpha(\Xi_c^0 \rightarrow \Xi^0 h^0)\alpha(\Xi^0 \rightarrow \Lambda\pi^0)\cos\theta_{\Xi^0}, \quad (1.1)$$

where $\alpha(\Xi^0 \rightarrow \Lambda\pi^0)$ is the asymmetry parameter for $\Xi^0 \rightarrow \Lambda\pi^0$ and $\cos\theta_{\Xi^0}$ is the angle between the Λ momentum vector and the direction opposite to the Ξ_c^0 momentum vector in the Ξ^0 rest frame. Predictions for $\alpha(\Xi_c^0 \rightarrow \Xi^0\pi^0)$ from various models are also listed in table 1. In addition to $\alpha(\Xi_c^0 \rightarrow B V)$ [2], $\alpha(\Xi_c^0 \rightarrow \Xi^-\pi^+)$ has also been measured by CLEO and Belle [21, 22].

In this paper, we present the first measurement of the branching fractions for $\Xi_c^0 \rightarrow \Xi^0\pi^0$, $\Xi_c^0 \rightarrow \Xi^0\eta$, and $\Xi_c^0 \rightarrow \Xi^0\eta'$ decays, and the asymmetry parameter of the $\Xi_c^0 \rightarrow \Xi^0\pi^0$ decay. The $\Xi_c^0 \rightarrow \Xi^-\pi^+$ decay is taken as the normalization mode for absolute branching fraction measurements. The signal yields used for branching fraction measurements are extracted from fits to the invariant mass distributions of fully reconstructed Ξ_c^0 candidates. The asymmetry parameter $\alpha(\Xi_c^0 \rightarrow \Xi^0\pi^0)$ is obtained from a linear fit to the Ξ_c^0 signal yield as a function of $\cos\theta_{\Xi^0}$. This analysis combines data samples with integrated luminosities of 980 fb^{-1} and 426 fb^{-1} collected with the Belle and Belle II detectors operating at the KEKB and SuperKEKB asymmetric-energy e^+e^- colliders, respectively. Charge-conjugate modes are implied throughout the paper.

2 Belle and Belle II detectors

The Belle detector [23, 24] operated from 1999 to 2010 at the KEKB asymmetric-energy e^+e^- collider [25, 26]. Belle was a large cylindrical solid-angle magnetic spectrometer that consisted of a silicon vertex detector, a central drift chamber, an array of aerogel threshold Cherenkov counters, a barrel-like arrangement of time-of-flight scintillation counters, an electromagnetic calorimeter (ECL) comprised of CsI(Tl) crystals located inside a superconducting solenoid coil that provided a 1.5 T axial magnetic field, and an iron flux return placed outside the coil, instrumented with resistive-plate chambers to detect K_L^0 mesons and to identify muons. A detailed description of the detector can be found in refs. [23, 24].

The Belle II detector [27] is located at the interaction point of the SuperKEKB asymmetric-energy e^+e^- collider [28]. Belle II is an upgraded version of the Belle detector and consists of several new subsystems and substantial upgrades to others. The new vertex detector includes two inner layers of pixel sensors and four outer layers of double-sided silicon microstrip sensors. For the data sample used in this analysis, the second pixel layer was incomplete, covering only one sixth of the azimuthal angle. A new central drift chamber surrounding the vertex detector is used to measure the momenta and electric charges of charged particles. A time-of-propagation detector in the barrel and an aerogel ring-imaging Cherenkov detector in the forward endcap provide information for the identification of charged particles, supplemented by ionization energy loss measurements in the central drift chamber. To cope with the higher beam-induced background environment at Belle II, the ECL readout electronics has been upgraded. The superconducting solenoid coil and the iron flux return for Belle are reused in Belle II, with some of the resistive-plate chambers in the K_L^0 and muon detector replaced by plastic scintillator modules.

The z axis of the cylindrical laboratory frame is defined as the central solenoid axis with the positive direction toward the e^- beam, common to Belle and Belle II.

3 Data sample

This measurement uses data recorded at center-of-mass (c.m.) energies at or near the $\Upsilon(1S)$, $\Upsilon(2S)$, $\Upsilon(3S)$, $\Upsilon(4S)$, and $\Upsilon(5S)$ resonances by the Belle detector, and at or near the $\Upsilon(4S)$ and at 10.75 GeV by the Belle II detector. The data samples correspond to integrated luminosities of 980 fb^{-1} and 426 fb^{-1} for Belle and Belle II, respectively.

Monte Carlo (MC) samples of simulated events are used to optimize signal selection criteria, calculate the reconstruction efficiency, and investigate possible background sources. Signal events are generated using the PYTHIA [29, 30] and EVTGEN [31] software packages via $e^+e^- \rightarrow c\bar{c}$, where one of the charm quarks is required to hadronize into a Ξ_c^0 baryon. Simulated $\Xi_c^0 \rightarrow \Xi^0 h^0 / \Xi^- \pi^+$ decays are generated with a phase space model. To obtain the correct reconstruction and selection efficiency, the simulated signal samples are weighted according to the measured values of α . Due to the small sample size, α is not measured for $\Xi_c^0 \rightarrow \Xi^0 \eta^{(\prime)}$, so the corresponding simulated signal samples are not weighted. Background samples of $\Upsilon(4S) \rightarrow B^+ B^-$ and $B^0 \bar{B}^0$ decays at Belle and Belle II, as well as $\Upsilon(5S) \rightarrow B_s^{(*)0} \bar{B}_s^{(*)0}$ decays at Belle, are generated using EVTGEN and PYTHIA. The continuum background from $e^+e^- \rightarrow q\bar{q}$ processes, where q indicates a u , d , c , or s quark, is generated by the KKMC [32] software package, with PYTHIA used for hadronization and EVTGEN for subsequent decays of hadrons. Final state radiation effects are accounted for using the PHOTOS package [33]. Simulation of the detector response uses the GEANT3 [34] and GEANT4 [35] software packages for Belle and Belle II, respectively.

4 Selection criteria

We reconstruct the decays $\Xi_c^0 \rightarrow \Xi^0 \pi^0$, $\Xi^0 \eta$, $\Xi^0 \eta'$, and $\Xi^- \pi^+$, followed by the decays $\Xi^0 \rightarrow \Lambda \pi^0$, $\Xi^- \rightarrow \Lambda \pi^-$, $\Lambda \rightarrow p \pi^-$, $\eta' \rightarrow \pi^+ \pi^- \eta$, and $\pi^0 / \eta \rightarrow \gamma \gamma$. The Belle II software [36] is used for event reconstruction of both samples, taking advantage of software improvements in Belle II. The Belle data are converted to the Belle II data format [37]. The selection criteria are nearly identical for Belle and Belle II. A global decay chain vertex fit is applied for each mode using the TreeFit algorithm [38].

For reconstructed charged particles not originating from long-lived Ξ^- and Λ baryon decays, the impact parameters, which are the distances of closest approach from the reconstructed trajectory perpendicular to and along the z axis with respect to the nominal interaction point, are required to be less than 0.1 cm and 2 cm, respectively, to suppress misreconstructed tracks and beam background. Charged particles are identified using the likelihood \mathcal{L}_i for each particle hypothesis i based on the information provided by the relevant sub-detector systems. For Belle data, the pion, kaon, and proton particle identification (PID) uses information from the drift chamber, Cherenkov detectors, and the time-of-flight detector [39]. Information from all subdetectors except the pixel detector is used to determine PID likelihoods for Belle II data.

The reconstruction and selection of Ξ^- and Ξ^0 candidates are similar to those described in refs. [40–42]. The Λ candidates are reconstructed via the $\Lambda \rightarrow p\pi^-$ decay, where the proton is identified by a PID requirement $\mathcal{L}_p/(\mathcal{L}_p + \mathcal{L}_\pi) > 0.2$ and $\mathcal{L}_p/(\mathcal{L}_p + \mathcal{L}_K) > 0.2$ for Belle and $\mathcal{L}_p/(\mathcal{L}_p + \mathcal{L}_e + \mathcal{L}_\mu + \mathcal{L}_\pi + \mathcal{L}_K + \mathcal{L}_d) > 0.01$ for Belle II. The selection efficiency of the PID requirement and the probability of misidentifying a hadron, depending on the particle species and kinematic properties, are approximately 90% (94%) and 1% (1%), respectively, at Belle (Belle II) in this case. The invariant mass of the reconstructed Λ candidate must be within $3.5 \text{ MeV}/c^2$, corresponding to approximately two times the mass resolution, σ , of the known mass [43]. Each π^- candidate from the Ξ^- decay is required to have a transverse momentum greater than $50 \text{ MeV}/c$ to remove backgrounds from low-momentum pions. Candidate π^0 's from Ξ^0 decays are reconstructed from pairs of photons selected from energy deposits in the ECL (clusters). To suppress low-momentum and fake photons, each photon candidate is required to have energy greater than: 30 MeV in the ECL barrel region ($-0.63 < \cos\theta < 0.85$); 50 (80) MeV for Belle (Belle II) in the forward endcap ($0.85 < \cos\theta < 0.98$); and 50 (60) MeV in the backward endcap ($-0.91 < \cos\theta < -0.63$), where θ is the polar angle in the laboratory frame. The reconstructed invariant mass of the photon pair is required to be within $11.6 \text{ MeV}/c^2$ (approximately 2σ) of the known π^0 mass. The momenta of the π^0 candidates in the laboratory frame are required to exceed $0.25 \text{ GeV}/c$. Candidate Ξ^- and Ξ^0 baryons are formed from $\Lambda\pi^-$ and $\Lambda\pi^0$ combinations, respectively. A vertex fit is applied to the entire $\Xi^{-(0)}$ decay chain, including subsequent decay products, with the $p\pi$ and diphoton masses constrained to match the known Λ and π^0 masses [43].

The reconstructed Ξ^- and Ξ^0 masses are required to be within $6 \text{ MeV}/c^2$ and $5 \text{ MeV}/c^2$ (approximately 3σ and 1.5σ) of their known masses, respectively. These selections are optimized by maximizing the figure-of-merit $N_{\text{sig}}/\sqrt{N_{\text{sig}} + N_{\text{bkg}}}$, where N_{sig} and N_{bkg} are the numbers of Ξ_c^0 signal events and background events in the Ξ_c^0 signal region. The Ξ_c^0 signal regions are the Ξ_c^0 invariant mass ranges of (2.716, 2.766), (2.25, 2.65), (2.3, 2.6), and (2.42, 2.53) GeV/c^2 for the $\Xi_c^0 \rightarrow \Xi^- \pi^+$, $\Xi_c^0 \rightarrow \Xi^0 \pi^0$, $\Xi_c^0 \rightarrow \Xi^0 \eta$, and $\Xi_c^0 \rightarrow \Xi^0 \eta'$ decay modes, respectively. These regions contain more than 95% of the simulated signals. For the normalization mode, N_{sig} and N_{bkg} are obtained via an unbinned extended maximum-likelihood (EML) fit to the $\Xi^- \pi^+$ invariant mass spectrum in data. For the signal modes, N_{sig} is the number of expected signal events using the branching fraction predictions in ref. [17] and N_{bkg} is the number of background events from the simulated samples of size similar to our data. The optimized Ξ^0 mass requirements do not strongly depend on h^0 and assumed branching fractions, hence we use the same mass requirements for all three signal modes.

ECL clusters are used to reconstruct photons to form π^0 , η , and η' candidates from Ξ_c^0 decays. To reduce the background originating from neutral hadrons, we require the energy deposited in a 3×3 matrix of crystals centered on the leading-energy crystal to be 80% or more of the energy deposited in the surrounding 5×5 matrix, in which, different with Belle, outer corner crystals are not considered in Belle II data. Candidate π^0 and η mesons are reconstructed by combining pairs of photons, whose energies are required to be greater than 80, 300, and 150 MeV for $\Xi_c^0 \rightarrow \Xi^0 \pi^0$, $\Xi_c^0 \rightarrow \Xi^0 \eta$, and $\Xi_c^0 \rightarrow \Xi^0 \eta'$, respectively. We

reconstruct η' candidates by combining an η candidate with a pair of oppositely-charged pions, which must satisfy a PID requirement of $\mathcal{L}_\pi/(\mathcal{L}_\pi + \mathcal{L}_K) > 0.2$ with identification efficiencies of 99% and misidentification probabilities of 1% for both Belle and Belle II. Loose mass windows are then used to select π^0 , η or η' candidates, with ranges of (0.08, 0.18), (0.4, 0.7) or (0.8, 1.1) GeV/ c^2 , respectively. A requirement on the kinematic mass-constrained fit quality is applied, $\chi^2 < 5$ for the h^0 candidate. The momentum in the c.m. frame for the selected h^0 candidate from the Ξ_c^0 is required to exceed 0.8 GeV/ c in order to suppress background with low momentum neutral particles.

The Ξ_c^0 candidates are reconstructed either by combining a Ξ^- candidate with a π^+ candidate, or by combining a Ξ^0 candidate with a π^0 , η , or η' candidate. To identify the π^+ candidate, we use the selections $\mathcal{L}_\pi/(\mathcal{L}_\pi + \mathcal{L}_K) > 0.2$ and $\mathcal{L}_\pi/(\mathcal{L}_\pi + \mathcal{L}_p) > 0.2$, with signal efficiencies of 96% and 94% for Ξ_c^0 selection, and misidentification probabilities of 3% and 2% for Belle and Belle II, respectively. To suppress backgrounds, especially those from B -meson decays, we require the scaled momentum, $x_p = p_{\Xi_c^0}^* c / \sqrt{s/4 - M^2(\Xi_c^0)c^4}$, of the Ξ_c^0 candidate to be greater than 0.55, where $p_{\Xi_c^0}^*$ is the momentum of Ξ_c^0 candidate in the c.m. frame, s is the square of c.m. energy, and $M(\Xi_c^0)$ is the invariant mass of the Ξ_c^0 candidate. The selection criteria for photon energies, h^0 momentum, $\chi^2(h^0)$, and x_p are optimized by maximizing the figure-of-merit as indicated above. Optimizing the selection criteria with an alternative parameterization $\varepsilon/(5/2 + \sqrt{N_{\text{bkg}}})$ [44], where ε is the reconstruction efficiency for $\Xi_c^0 \rightarrow \Xi^0 h^0$, gives consistent results.

The fractions of events that have multiple candidate events in signal simulations are about 2% (3%), 6% (7%), 6% (7%), and 7% (9%) for $\Xi_c^0 \rightarrow \Xi^- \pi^+$, $\Xi_c^0 \rightarrow \Xi^0 \pi^0$, $\Xi_c^0 \rightarrow \Xi^0 \eta$, and $\Xi_c^0 \rightarrow \Xi^0 \eta'$, respectively in Belle (Belle II) data. These values are consistent with the multiple candidate rates observed in the data. All $\Xi_c^0 \rightarrow \Xi^- \pi^+$ candidates are retained after applying these selections. For $\Xi_c^0 \rightarrow \Xi^0 h^0$ events with a single Ξ^0 candidate but multiple h^0 candidates, the h^0 candidate with the minimum mass-constrained fit χ^2 is selected. If an event has multiple Ξ^0 candidates, one is selected at random. This candidate selection procedure yields simulated signal efficiencies for events with multiple candidates of 53% (46%), 51% (42%), and 54% (44%) for $\Xi_c^0 \rightarrow \Xi^0 \pi^0$, $\Xi_c^0 \rightarrow \Xi^0 \eta$, and $\Xi_c^0 \rightarrow \Xi^0 \eta'$, respectively, at Belle (Belle II). After this selection, the overall purities in signal regions of the simulated samples increase by 2% (4%), 2% (4%), and 3% (5%) for $\Xi_c^0 \rightarrow \Xi^0 \pi^0$, $\Xi_c^0 \rightarrow \Xi^0 \eta$, and $\Xi_c^0 \rightarrow \Xi^0 \eta'$, respectively in Belle (Belle II) data.

5 Branching fractions for $\Xi_c^0 \rightarrow \Xi^0 \pi^0$, $\Xi_c^0 \rightarrow \Xi^0 \eta$, and $\Xi_c^0 \rightarrow \Xi^0 \eta'$

Figure 2 shows the $\Lambda\pi^-$, $\Lambda\pi^0$, $\gamma\gamma$, and $\pi^+\pi^-\eta$ invariant mass distributions, along with the fit results, for Ξ_c^0 candidates in the signal region using Belle and Belle II data. All event selection criteria described in Section 4 are applied, except for the candidate selection procedure and the selection on the corresponding invariant mass region or mass-constrained fit χ^2 . We perform binned EML fits to the invariant mass distributions of the intermediate Ξ and h^0 states, where the signal probability density functions (PDFs) are parameterized using a double-Gaussian function with a common mean for the Ξ^- , Ξ^0 , and η' candidates, and a Crystal Ball function [45] for the π^0 and η candidates. The smooth combinatorial

backgrounds are described with a straight line for the $\gamma\gamma$, $\eta\pi^+\pi^-$ and $\Lambda\pi^-$ distributions, and a second-order polynomial for the $\Lambda\pi^0$ distributions. The solid and dashed arrows indicate the signal and sideband regions, respectively, for Ξ^- and Ξ^0 candidates.

The $\Xi^-\pi^+$ mass distributions for Ξ_c^0 candidates selected as described in sec. 4 are shown in figure 3, together with the results of an unbinned EML fit. In the fit, the signal shape for Ξ_c^0 candidates is parameterized by a double-Gaussian function with a common mean and the background shape is described by a straight line. All signal and background parameters are floating in the fit. The distributions of pulls, $(N_{\text{data}} - N_{\text{fit}})/\sigma_{\text{data}}$, are also displayed in figure 3, where N_{data} is the number of entries in each bin from data, N_{fit} is the fit result in each bin, and σ_{data} is the uncertainty on N_{data} . The fitted signal yields are summarized in table 2.

Distributions of $\Xi^0 h^0$ masses of Ξ_c^0 candidates reconstructed in data and selected as described in sec. 4 are shown in figure 4 with the results of an unbinned EML fit overlaid. The fit PDF includes terms for the signal (\mathcal{F}_{sig}), broken-signal ($\mathcal{F}_{\text{broken}}$) and smooth background (\mathcal{F}_{bkg}) contributions:

$$\mathcal{F} = n_{\text{sig}}\mathcal{F}_{\text{sig}} + n_{\text{broken}}\mathcal{F}_{\text{broken}} + n_{\text{bkg}}\mathcal{F}_{\text{bkg}}, \quad (5.1)$$

where n_{sig} , n_{broken} , and n_{bkg} are the numbers of Ξ_c^0 signal events, broken-signal events, and smooth background events, respectively. Here the broken-signal events are those for which at least one of the final state particles, primarily a photon, is not associated with the signal decay. The values of n_{sig} and n_{bkg} are allowed to float in the fit, while the ratios of n_{broken} to n_{sig} are fixed to the fractions from signal MC simulation and are 11.6% (16.0%), 13.3% (18.4%), and 13.3% (21.0%) for $\Xi_c^0 \rightarrow \Xi^0\pi^0$, $\Xi_c^0 \rightarrow \Xi^0\eta$, and $\Xi_c^0 \rightarrow \Xi^0\eta'$ decay modes, respectively, at Belle (Belle II). Studies based on associating MC simulation generator information to events reconstructed from simulation [46] and $M(\Xi^0 h^0)$ distributions from the Ξ^0 data sidebands show no evidence of peaking backgrounds. The signal PDF in the $\Xi_c^0 \rightarrow \Xi^0\pi^0$ mode is described by two Crystal Ball functions [45] with a common mean, convolved with a Gaussian function to take into account the difference in mass resolution from the simulated events. For the $\Xi_c^0 \rightarrow \Xi^0\eta$ and $\Xi_c^0 \rightarrow \Xi^0\eta'$ modes, the signal PDF is modeled using double-Gaussian functions with a common mean. All the signal PDF parameters are fixed to the values obtained from signal simulation, except for the mean value of the signal PDF and the width of the Gaussian resolution function, which are determined in the fit to data. The width is found to be 11.1 ± 2.0 (8.7 ± 2.7) MeV/ c^2 in Belle (Belle II), where the uncertainty is statistical only. The $\mathcal{F}_{\text{broken}}$ term is a non-parametric kernel estimation PDF [47] obtained from simulations. The \mathcal{F}_{bkg} PDF is parameterized by a third-order polynomial for the $\Xi_c^0 \rightarrow \Xi^0\pi^0$ mode and by a straight line for the $\Xi_c^0 \rightarrow \Xi^0\eta$ and $\Xi_c^0 \rightarrow \Xi^0\eta'$ modes. All of the parameters for \mathcal{F}_{bkg} are allowed to vary in the fit. Further validation of the fit using simulation confirms that the fit results are unbiased and have Gaussian uncertainties. The reconstruction efficiencies and fit results are listed in table 2. The statistical significances for $\Xi_c^0 \rightarrow \Xi^0\pi^0$, $\Xi_c^0 \rightarrow \Xi^0\eta$, and $\Xi_c^0 \rightarrow \Xi^0\eta'$ are greater than 10σ (10σ), 6.2σ (6.7σ), and 5.9σ (2.4σ) in Belle (Belle II), respectively, calculated using $\sqrt{-2\ln(\mathcal{L}_0/\mathcal{L}_{\text{max}})}$, where \mathcal{L}_0 and \mathcal{L}_{max} are the maximized likelihoods without and with the signal component, respectively.

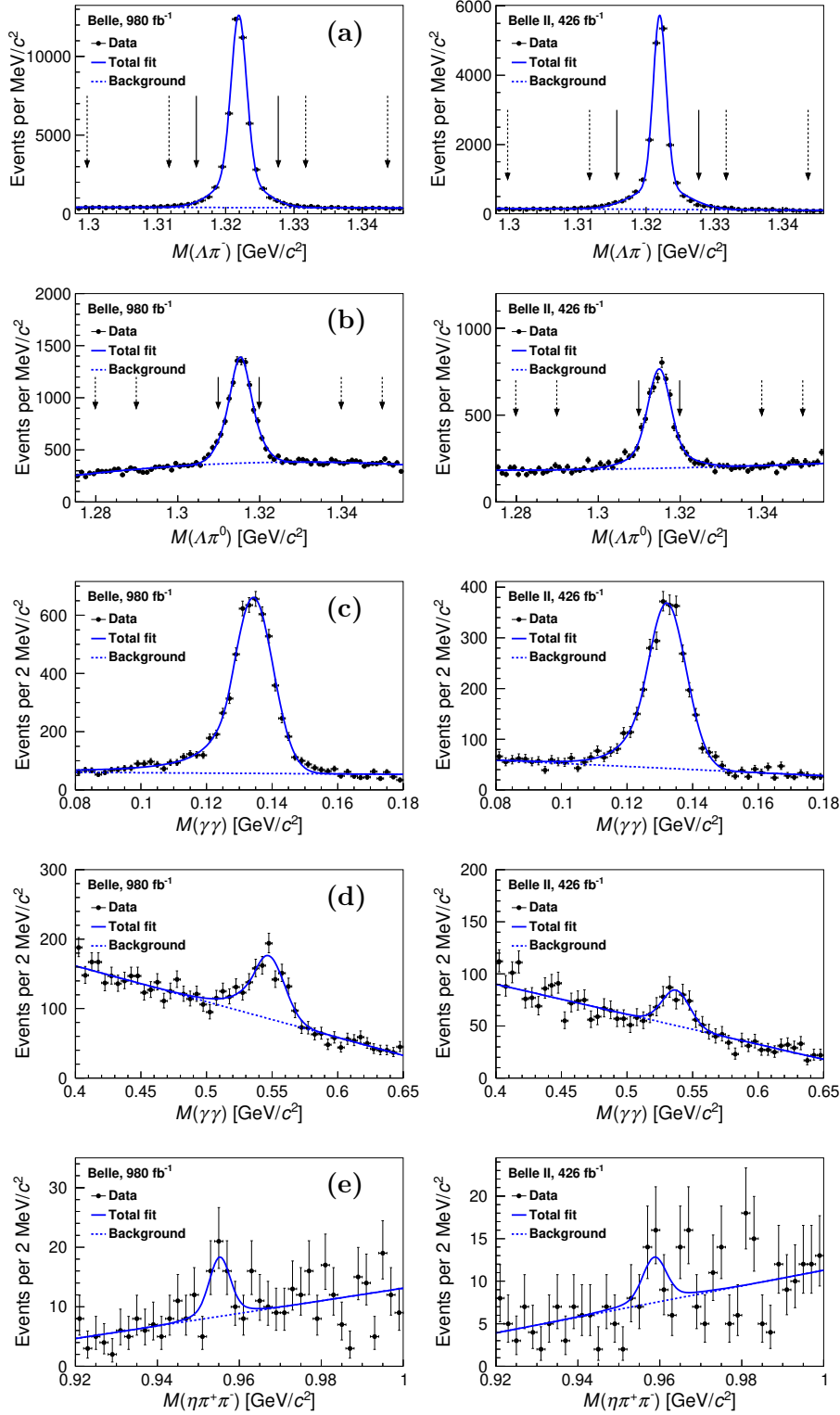


Figure 2. Invariant mass distributions of (a) $\Lambda\pi^-$ for Ξ^- candidates, (b) $\Lambda\pi^0$ for Ξ^0 candidates, (c) $\gamma\gamma$ for π^0 candidates, (d) $\gamma\gamma$ for η candidates, and (e) $\pi^+\pi^-\eta$ for η' candidates in the Ξ_c signal regions. For each distribution, the left plot shows the result for the Belle sample and the right plot shows that for the Belle II data. The markers with error bars represent the data, the solid curves show the total fit, and the dashed curves show the smooth background component of the fit. The solid and dashed arrows show the signal and sideband regions for $\Xi_c^{-(0)}$ candidates, respectively.

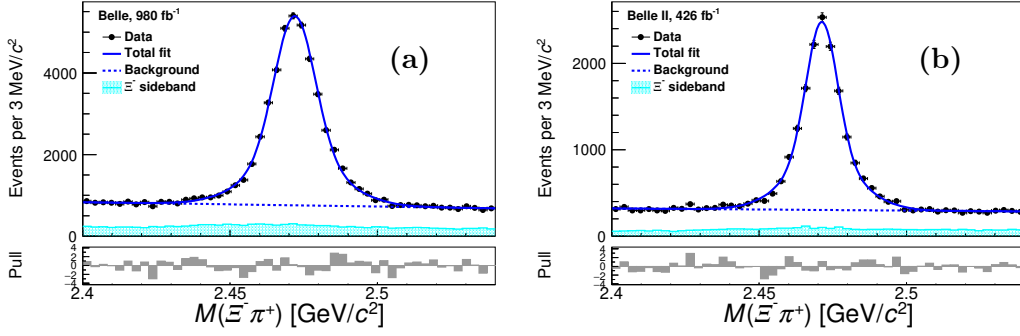


Figure 3. Invariant mass distributions of $\Xi^- \pi^+$ from (a) Belle and (b) Belle II data. The markers with error bars represent the data, the solid blue curves show the fit results, and the dashed blue curves show the background component of the fit. The cyan histograms are the data from Ξ^- mass sidebands.

Table 2. Observed Ξ_c^0 signal yields and reconstruction efficiencies for various modes, where uncertainties are statistical only.

Mode	Belle yield	$\varepsilon_{\text{Belle}}$ (%)	Belle II yield	$\varepsilon_{\text{Belle II}}$ (%)
$\Xi_c^0 \rightarrow \Xi^- \pi^+$	$(363 \pm 3) \times 10^2$	13.92 ± 0.05	$(137 \pm 2) \times 10^2$	13.38 ± 0.03
$\Xi_c^0 \rightarrow \Xi^0 \pi^0$	1315 ± 66	1.09 ± 0.01	869 ± 46	1.71 ± 0.01
$\Xi_c^0 \rightarrow \Xi^0 \eta$	81 ± 15	0.80 ± 0.01	60 ± 11	1.12 ± 0.01
$\Xi_c^0 \rightarrow \Xi^0 \eta'$	23 ± 6	0.46 ± 0.01	8 ± 4	0.81 ± 0.01

The ratios of branching fractions to the normalization mode $\Xi_c^0 \rightarrow \Xi^- \pi^+$ are calculated via

$$\begin{aligned}
\frac{\mathcal{B}(\Xi_c^0 \rightarrow \Xi^0 \pi^0)}{\mathcal{B}(\Xi_c^0 \rightarrow \Xi^- \pi^+)} &= \frac{N_{\Xi^0 \pi^0} \varepsilon_{\Xi^- \pi^+}}{\varepsilon_{\Xi^0 \pi^0} N_{\Xi^- \pi^+}} \times \frac{\mathcal{B}(\Xi^- \rightarrow \Lambda \pi^-)}{\mathcal{B}(\Xi^0 \rightarrow \Lambda \pi^0) \mathcal{B}(\pi^0 \rightarrow \gamma \gamma) \mathcal{B}(\pi^0 \rightarrow \gamma \gamma)}, \\
\frac{\mathcal{B}(\Xi_c^0 \rightarrow \Xi^0 \eta)}{\mathcal{B}(\Xi_c^0 \rightarrow \Xi^- \pi^+)} &= \frac{N_{\Xi^0 \eta} \varepsilon_{\Xi^- \pi^+}}{\varepsilon_{\Xi^0 \eta} N_{\Xi^- \pi^+}} \times \frac{\mathcal{B}(\Xi^- \rightarrow \Lambda \pi^-)}{\mathcal{B}(\Xi^0 \rightarrow \Lambda \pi^0) \mathcal{B}(\pi^0 \rightarrow \gamma \gamma) \mathcal{B}(\eta \rightarrow \gamma \gamma)}, \\
\frac{\mathcal{B}(\Xi_c^0 \rightarrow \Xi^0 \eta')}{\mathcal{B}(\Xi_c^0 \rightarrow \Xi^- \pi^+)} &= \frac{N_{\Xi^0 \eta'} \varepsilon_{\Xi^- \pi^+}}{\varepsilon_{\Xi^0 \eta'} N_{\Xi^- \pi^+}} \times \frac{\mathcal{B}(\Xi^- \rightarrow \Lambda \pi^-)}{\mathcal{B}(\Xi^0 \rightarrow \Lambda \pi^0) \mathcal{B}(\pi^0 \rightarrow \gamma \gamma) \mathcal{B}(\eta' \rightarrow \pi^+ \pi^- \eta) \mathcal{B}(\eta \rightarrow \gamma \gamma)}.
\end{aligned} \tag{5.2}$$

Here, $N_{\Xi^0 \pi^0}$, $N_{\Xi^0 \eta}$, $N_{\Xi^0 \eta'}$, and $N_{\Xi^- \pi^+}$ are the Ξ_c^0 yields resulting from the fit; $\varepsilon_{\Xi^0 \pi^0}$, $\varepsilon_{\Xi^0 \eta}$, $\varepsilon_{\Xi^0 \eta'}$, and $\varepsilon_{\Xi^- \pi^+}$ are the corresponding reconstruction efficiencies; and the branching fractions are taken from ref. [43]. We combine the Belle and Belle II branching fraction ratios and uncertainties using the formulas in ref. [48],

$$\begin{aligned}
r &= \frac{r_1 \sigma_2^2 + r_2 \sigma_1^2}{\sigma_1^2 + \sigma_2^2 + (r_1 - r_2)^2 \epsilon_r^2}, \\
\sigma &= \sqrt{\frac{\sigma_1^2 \sigma_2^2 + (r_1^2 \sigma_2^2 + r_2^2 \sigma_1^2) \epsilon_r^2}{\sigma_1^2 + \sigma_2^2 + (r_1 - r_2)^2 \epsilon_r^2}},
\end{aligned} \tag{5.3}$$

where r_i , σ_i and ϵ_r are the branching fraction ratio, uncorrelated uncertainty, and relative correlated systematic uncertainty from each data sample, respectively. The branching frac-

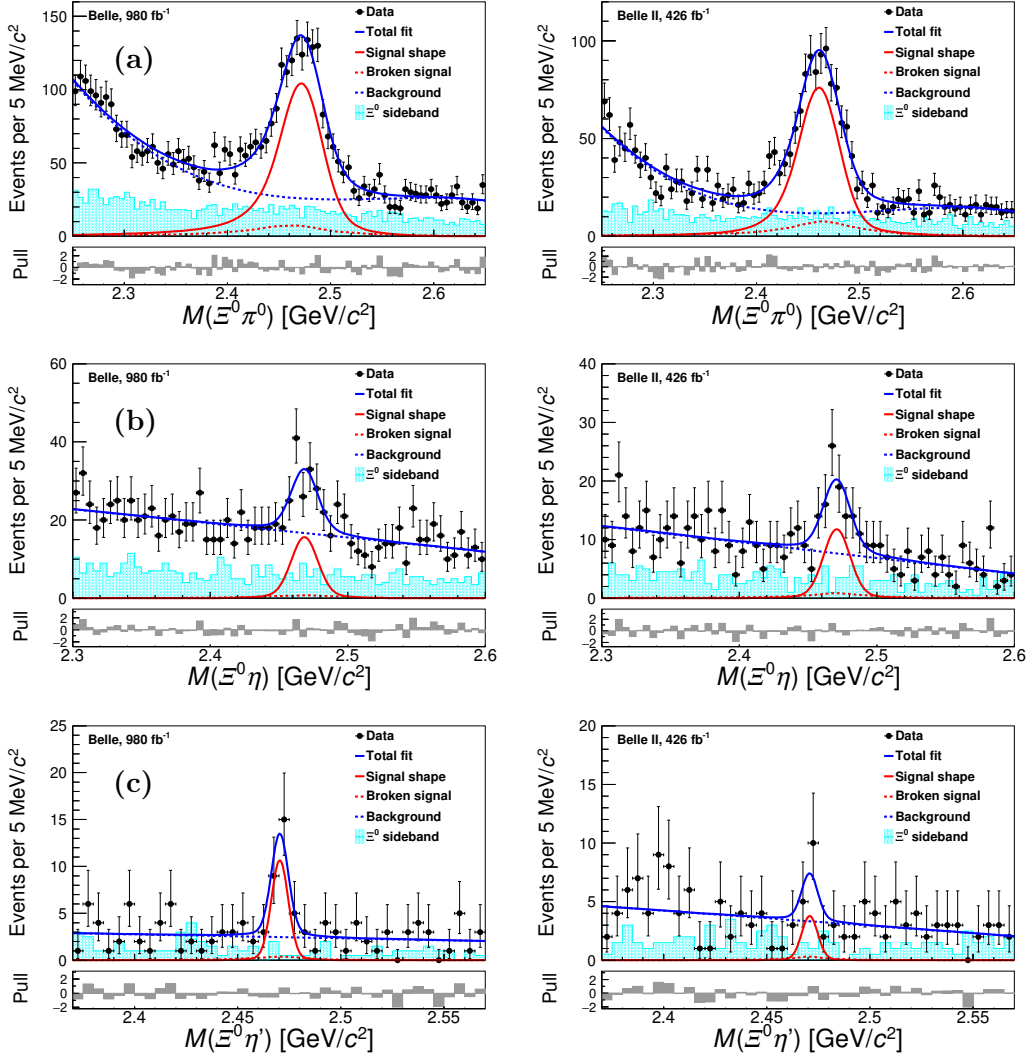


Figure 4. Invariant mass distributions of Ξ_c^0 candidates from (a) $\Xi_c^0 \rightarrow \Xi^0 \pi^0$, (b) $\Xi_c^0 \rightarrow \Xi^0 \eta$, and (c) $\Xi_c^0 \rightarrow \Xi^0 \eta'$ decays reconstructed in (left) Belle and (right) Belle II data. The markers with error bars represent the data. The solid blue curves, solid red curves, dashed red curves, and dashed blue curves show the total fit, signal shape, broken-signal shape, and smooth backgrounds, respectively. The cyan histograms show the data from the Ξ^0 mass sidebands.

tion ratios are summarized in table 3, where the first and second uncertainties are statistical and systematic, respectively. The systematic uncertainties are discussed in detail below.

6 Asymmetry parameter of $\Xi_c^0 \rightarrow \Xi^0 \pi^0$

Given the small sample sizes for the other modes, the asymmetry parameter is measured only for $\Xi_c^0 \rightarrow \Xi^0 \pi^0$. We divide the $\cos \theta_{\Xi^0}$ distribution into five equal sized non-overlapping contiguous intervals (bins). The Ξ_c^0 signal yield in each bin is obtained by fitting to the $M(\Xi^0 \pi^0)$ distribution where the signal shape is fixed to the result of a fit to the full sample,

Table 3. Branching fraction ratios of $\Xi_c^0 \rightarrow \Xi^0 h^0$ decays, where the first and second uncertainties are statistical and systematic, respectively.

Mode	Belle	Belle II	Combined
$\mathcal{B}(\Xi_c^0 \rightarrow \Xi^0 \pi^0)/\mathcal{B}(\Xi_c^0 \rightarrow \Xi^- \pi^+)$	$0.47 \pm 0.02 \pm 0.03$	$0.51 \pm 0.03 \pm 0.05$	$0.48 \pm 0.02 \pm 0.03$
$\mathcal{B}(\Xi_c^0 \rightarrow \Xi^0 \eta)/\mathcal{B}(\Xi_c^0 \rightarrow \Xi^- \pi^+)$	$0.10 \pm 0.02 \pm 0.01$	$0.14 \pm 0.02 \pm 0.02$	$0.11 \pm 0.01 \pm 0.01$
$\mathcal{B}(\Xi_c^0 \rightarrow \Xi^0 \eta')/\mathcal{B}(\Xi_c^0 \rightarrow \Xi^- \pi^+)$	$0.12 \pm 0.03 \pm 0.01$	$0.06 \pm 0.03 \pm 0.01$	$0.08 \pm 0.02 \pm 0.01$

Table 4. Values of the signal yield divided by reconstruction efficiency in $\cos \theta_{\Xi^0}$ bins for $\Xi_c^0 \rightarrow \Xi^0 \pi^0$ in the Belle and Belle II datasets.

$\cos \theta_{\Xi^0}$	$(-1.0, -0.6)$	$(-0.6, -0.2)$	$(-0.2, 0.2)$	$(0.2, 0.6)$	$(0.6, 1.0)$
Belle	$\frac{260 \pm 25}{1.40}$	$\frac{296 \pm 26}{1.29}$	$\frac{266 \pm 27}{1.14}$	$\frac{265 \pm 27}{0.99}$	$\frac{224 \pm 24}{0.71}$
Belle II	$\frac{176 \pm 18}{2.37}$	$\frac{167 \pm 18}{2.08}$	$\frac{194 \pm 20}{1.96}$	$\frac{151 \pm 17}{1.60}$	$\frac{176 \pm 17}{1.18}$

due to the limited sample size. The fits to $M(\Xi^0 \pi^0)$ spectra in $\cos \theta_{\Xi^0}$ bins are shown in appendix A. Table 4 lists the signal yields and reconstruction efficiencies in each $\cos \theta_{\Xi^0}$ bin. The final efficiency-corrected Ξ_c^0 signal yields in bins of $\cos \theta_{\Xi^0}$ for $\Xi_c^0 \rightarrow \Xi^0 \pi^0$ are shown in figure 5, together with the simultaneous fit result using Eq. (1.1) with a common value of the product $\alpha(\Xi_c^0 \rightarrow \Xi^0 h^0)\alpha(\Xi^0 \rightarrow \Lambda \pi^0)$ for the Belle and Belle II data samples. Using simplified simulated experiments generated with different α values, we test the α extraction procedure and find that it is unbiased. The product of asymmetry parameters is found to be $\alpha(\Xi_c^0 \rightarrow \Xi^0 \pi^0)\alpha(\Xi^0 \rightarrow \Lambda \pi^0) = 0.32 \pm 0.05(\text{stat})$. Taking $\alpha(\Xi^0 \rightarrow \Lambda \pi^0) = -0.349 \pm 0.009$ [43], we find $\alpha(\Xi_c^0 \rightarrow \Xi^0 \pi^0) = -0.90 \pm 0.15(\text{stat}) \pm 0.23(\text{syst})$, where the first uncertainty is statistical and the second is systematic. The values of $\alpha(\Xi_c^0 \rightarrow \Xi^0 \pi^0)$ extracted via individual fits to the Belle and Belle II data samples are -0.84 ± 0.21 and -0.98 ± 0.22 , where the uncertainties are statistical only, in good agreement with the result from the simultaneous fit.

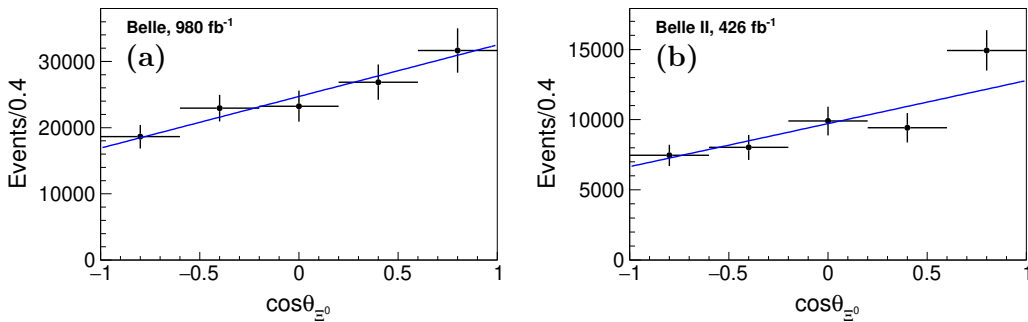


Figure 5. Efficiency-corrected Ξ_c^0 signal yields in bins of $\cos \theta_{\Xi^0}$ from the (a) Belle and (b) Belle II datasets. The lines show linear regression results.

Table 5. Fractional systematic uncertainties (%) on the relative branching-fraction results. The uncertainties in the last two rows, due to intermediate branching fractions and background shape, are common to Belle and Belle II; the other uncertainties are independent. Since the $\Lambda \rightarrow p\pi^-$ decay is reconstructed in each decay mode, the $\mathcal{B}(\Lambda \rightarrow p\pi^-)$ uncertainty and the uncertainty due to the $\Lambda \rightarrow p\pi^-$ reconstruction efficiency cancel in the ratio to the reference mode $\Xi_c^0 \rightarrow \Xi^- \pi^+$.

Source	$\frac{\mathcal{B}(\Xi_c^0 \rightarrow \Xi^0 \pi^0)}{\mathcal{B}(\Xi_c^0 \rightarrow \Xi^- \pi^+)}$		$\frac{\mathcal{B}(\Xi_c^0 \rightarrow \Xi^0 \eta)}{\mathcal{B}(\Xi_c^0 \rightarrow \Xi^- \pi^+)}$		$\frac{\mathcal{B}(\Xi_c^0 \rightarrow \Xi^0 \eta')}{\mathcal{B}(\Xi_c^0 \rightarrow \Xi^- \pi^+)}$	
	Belle	Belle II	Belle	Belle II	Belle	Belle II
Tracking	0.7	0.8	0.7	0.7	1.0	1.5
π^\pm PID	0.4	0.2	0.4	0.2	1.4	0.2
π^0 reconstruction	4.4	8.8	2.3	4.3	2.3	4.2
Photon reconstruction	-	-	4.0	2.0	4.0	1.9
Simulation sample size	0.8	0.7	0.9	0.9	1.2	1.0
α uncertainty	1.1	1.2	3.0	3.4	1.0	3.5
Ξ^0 signal mass window	0.5	2.0	0.5	2.0	0.5	2.0
Normalization mode sample size	1.0	1.3	1.0	1.3	1.0	1.3
Broken-signal ratio ($n_{\text{broken}}/n_{\text{sig}}$)	2.1	1.5	3.5	3.6	3.6	5.7
Broken-signal PDF	0.2	0.1	7.3	7.5	2.0	1.1
Mass resolution	-	-	7.2	7.0	2.4	1.4
Intermediate states \mathcal{B}	-	-	0.5	0.5	1.3	1.3
Background shape	4.9	4.9	9.2	9.2	6.8	6.8
Total	7.2	10.6	15.3	15.6	9.9	11.2

7 Systematic uncertainties

7.1 Branching fraction ratios

The sources of systematic uncertainties for the branching fraction ratio measurements include those related to the efficiency, the intermediate branching fractions, and the fit procedure. Table 5 summarizes the systematic uncertainties, where the total uncertainty is determined from a quadratic sum of the uncertainties from each source.

The systematic uncertainty due to the efficiency includes effects due to the detection efficiency, simulation sample size, α uncertainty, and the mass window for the Ξ^0 signal. The detection efficiencies determined in simulations are corrected by multiplicative data-to-simulation ratios determined from control data samples. The correction factors and uncertainties include those from track-finding efficiency, obtained from the control samples of $D^{*+} \rightarrow D^0(\rightarrow K_S^0 \pi^+ \pi^-) \pi^+$ at Belle and $\bar{B}^0 \rightarrow D^{*+}(\rightarrow D^0 \pi^+) \pi^-$ and $e^+ e^- \rightarrow \tau^+ \tau^-$ at Belle II; charged pion identification, obtained from the $D^{*+} \rightarrow D^0(\rightarrow K^- \pi^+) \pi^+$ control sample at Belle and Belle II; π^0 reconstruction, obtained from the $\tau \rightarrow \pi^- \pi^0 \nu_\tau$ control sample at Belle and the $D^0 \rightarrow K^- \pi^+ \pi^0$ control sample at Belle II; and photon reconstruction, obtained from control samples of radiative Bhabhas at Belle and radiative muon-pairs at Belle II. The relative systematic uncertainty due to the size of the simulated sample is calculated using a binomial uncertainty estimate. For the $\Xi^0 \pi^0$ channel, we use the change in efficiency due to variations of the measured value of α by one standard deviation as a systematic uncertainty; for the other channels we use the difference in efficiencies observed when assuming the extreme values $\alpha = +1$ or -1 . The uncertainty due to the Ξ^0 sig-

nal region choice is calculated from the difference between the selected signal fractions in simulation and data. Since the $\chi^2(h^0)$ distributions from sideband-subtracted data and simulations are consistent, the efficiency differences on the $\chi^2 < 5$ requirement between data and simulations are less than 1%, and thus the uncertainty due to the χ^2 criterion is neglected here.

The systematic uncertainties due to the intermediate branching fractions are taken to be the uncertainties on the world-average values and treated as correlated uncertainties, which are common to Belle and Belle II. Only the uncertainties for $\mathcal{B}(\eta \rightarrow \gamma\gamma)$ (0.5%) and $\mathcal{B}(\eta' \rightarrow \pi^+\pi^-\eta)\mathcal{B}(\eta \rightarrow \gamma\gamma)$ (1.3%) contribute for $\Xi_c^0 \rightarrow \Xi^0\eta$ and $\Xi_c^0 \rightarrow \Xi^0\eta'$, respectively. The uncertainties for other intermediate branching fractions are smaller than 0.1% and are neglected. The 22.4% uncertainty on $\mathcal{B}(\Xi_c^0 \rightarrow \Xi^-\pi^+)$ is treated as an independent systematic uncertainty in the measurement of the absolute branching fractions.

The uncertainties due to the fit procedure are determined by taking the difference between the $\Xi_c^0 \rightarrow \Xi^0 h^0$ signal yield in the nominal fit and the signal yields in fits with the following modifications: (1) changing the order of polynomial for the smooth background, (2) floating the ratio of n_{broken} to n_{sig} , (3) convolving the signal shapes of $\Xi_c^0 \rightarrow \Xi^0 \eta^{(\prime)}$ with a Gaussian function with a floating width, and (4) changing the broken-signal PDF smoothed by ‘rookepdf’ to ‘roohistpdf’ [47, 49], corresponding to two algorithms for PDF estimation from simulated samples. The background function is common to the two experiments, and the corresponding uncertainty is extracted from a simultaneous fit for Ξ_c^0 signal yield in Belle and Belle II data. Facing the worst signal-background ratio, the fitting uncertainties for $\Xi_c^0 \rightarrow \Xi^0\eta$ channel are larger than other two channels of $\Xi_c^0 \rightarrow \Xi^0\pi^0$ and $\Xi_c^0 \rightarrow \Xi^0\eta'$. The total systematic uncertainty is obtained by adding the contributions from each source in quadrature.

7.2 Asymmetry parameter

The sources of the systematic uncertainty on the asymmetry parameter measurement include the uncertainty on $\alpha(\Xi^0 \rightarrow \Lambda\pi^0)$, the number of $\cos\theta_{\Xi^0}$ bins, and the uncertainties due to the fit procedure. The relative uncertainty on $\alpha(\Xi^0 \rightarrow \Lambda\pi^0) = -0.349 \pm 0.009$ [43] is 2.6%. We change the number of $\cos\theta_{\Xi^0}$ bins from 5 to 4 and 6, and the difference in the extracted asymmetry parameter, 0.14, is taken as the associated systematic uncertainty. The uncertainty from the fit procedure, 0.18, is determined using a similar procedure as for those in the branching fraction ratio measurements, where the width of the convolved Gaussian function is varied by $\pm 1\sigma$ to obtain the uncertainty from reconstruction resolution. We find that the systematic uncertainty due to the efficiency can be neglected since the efficiency is a multiplicative scale factor for the efficiency-corrected Ξ_c^0 signal yield in each $\cos\theta_{\Xi^0}$ bin and does not change the α value. As noted in section 3, the simulated signal sample is weighted to match the observed value of α . When the weights are changed by the corresponding uncertainties ($\pm 1\sigma$), the α measurement changes by less than 0.01: this effect is neglected. The measurement is insensitive to the Ξ_c^0 polarization, and no systematic uncertainty is included from this source [2, 21]. The systematic uncertainties from all sources are added in quadrature to obtain a value of 0.23.

8 Summary and discussion

We report the first measurements on $\Xi_c^0 \rightarrow \Xi^0 h^0$ decays, using the combined Belle and Belle II data samples corresponding to a total integrated luminosity of about 1.4 ab^{-1} . The branching fractions of $\Xi_c^0 \rightarrow \Xi^0 h^0$ relative to $\mathcal{B}(\Xi_c^0 \rightarrow \Xi^- \pi^+)$ are measured to be

$$\mathcal{B}(\Xi_c^0 \rightarrow \Xi^0 \pi^0)/\mathcal{B}(\Xi_c^0 \rightarrow \Xi^- \pi^+) = 0.48 \pm 0.02(\text{stat}) \pm 0.03(\text{syst}), \quad (8.1)$$

$$\mathcal{B}(\Xi_c^0 \rightarrow \Xi^0 \eta)/\mathcal{B}(\Xi_c^0 \rightarrow \Xi^- \pi^+) = 0.11 \pm 0.01(\text{stat}) \pm 0.01(\text{syst}), \quad (8.2)$$

and

$$\mathcal{B}(\Xi_c^0 \rightarrow \Xi^0 \eta')/\mathcal{B}(\Xi_c^0 \rightarrow \Xi^- \pi^+) = 0.08 \pm 0.02(\text{stat}) \pm 0.01(\text{syst}), \quad (8.3)$$

where the first uncertainties are statistical and the second are systematic. Taking $\mathcal{B}(\Xi_c^0 \rightarrow \Xi^- \pi^+) = (1.43 \pm 0.27)\%$ [43], the absolute branching fractions are measured to be

$$\mathcal{B}(\Xi_c^0 \rightarrow \Xi^0 \pi^0) = (6.9 \pm 0.3(\text{stat}) \pm 0.5(\text{syst}) \pm 1.3(\text{norm})) \times 10^{-3}, \quad (8.4)$$

$$\mathcal{B}(\Xi_c^0 \rightarrow \Xi^0 \eta) = (1.6 \pm 0.2(\text{stat}) \pm 0.2(\text{syst}) \pm 0.3(\text{norm})) \times 10^{-3}, \quad (8.5)$$

and

$$\mathcal{B}(\Xi_c^0 \rightarrow \Xi^0 \eta') = (1.2 \pm 0.3(\text{stat}) \pm 0.1(\text{syst}) \pm 0.2(\text{norm})) \times 10^{-3}, \quad (8.6)$$

where the third uncertainty is from $\mathcal{B}(\Xi_c^0 \rightarrow \Xi^- \pi^+)$. We measure the asymmetry parameter

$$\alpha(\Xi_c^0 \rightarrow \Xi^0 \pi^0) = -0.90 \pm 0.15(\text{stat}) \pm 0.23(\text{syst}) \quad (8.7)$$

for the first time. Due to the limited data sample size, the asymmetry parameters for $\Xi_c^0 \rightarrow \Xi^0 \eta$ and $\Xi_c^0 \rightarrow \Xi^0 \eta'$ are not measured, but will become accessible with the larger data samples to be collected by Belle II in the future.

Comparing with the theoretical predictions summarized in table 1, a recent result [17] based on the $\text{SU}(3)_F$ -breaking model is consistent with each measured $\mathcal{B}(\Xi_c^0 \rightarrow \Xi^0 h^0)$. The measured value of $\alpha(\Xi_c^0 \rightarrow \Xi^0 \pi^0)$ is consistent with predictions based on the pole model [8, 10], CA [11], and $\text{SU}(3)_F$ flavor symmetry [13] approaches. The central values of our measurements of the absolute branching fractions and asymmetry parameter of $\Xi_c^0 \rightarrow \Xi^0 \pi^0$, indicate that the covariant confined quark model [5, 6] is mildly disfavored for each result, and disagree with the predictions by more than 2σ for the following: (1) $\mathcal{B}(\Xi_c^0 \rightarrow \Xi^0 \pi^0)$ in refs. [8, 10, 15, 18]; (2) $\mathcal{B}(\Xi_c^0 \rightarrow \Xi^0 \eta)$ in refs. [10, 13, 19, 20]; (3) $\mathcal{B}(\Xi_c^0 \rightarrow \Xi^0 \eta')$ in refs. [9, 14, 19, 20]; and (4) $\alpha(\Xi_c^0 \rightarrow \Xi^0 \pi^0)$ in refs. [7, 9, 17–20]. The results for the ratios, (8.1), (8.2), and (8.3), are independent of the Ξ_c^0 absolute branching fraction scale and may also be compared to theoretical models.

Acknowledgments

This work, based on data collected using the Belle II detector, which was built and commissioned prior to March 2019, was supported by Higher Education and Science Committee of the Republic of Armenia Grant No. 23LCG-1C011; Australian Research Council and Research Grants No. DP200101792, No. DP210101900, No. DP210102831, No. DE220100462,

No. LE210100098, and No. LE230100085; Austrian Federal Ministry of Education, Science and Research, Austrian Science Fund No. P 34529, No. J 4731, No. J 4625, and No. M 3153, and Horizon 2020 ERC Starting Grant No. 947006 “InterLeptons”; Natural Sciences and Engineering Research Council of Canada, Compute Canada and CANARIE; National Key R&D Program of China under Contract No. 2022YFA1601903, National Natural Science Foundation of China and Research Grants No. 11575017, No. 11761141009, No. 11705209, No. 11975076, No. 12135005, No. 12150004, No. 12161141008, and No. 12175041, and Shandong Provincial Natural Science Foundation Project ZR2022JQ02; the Czech Science Foundation Grant No. 22-18469S and Charles University Grant Agency project No. 246122; European Research Council, Seventh Framework PIEF-GA-2013-622527, Horizon 2020 ERC-Advanced Grants No. 267104 and No. 884719, Horizon 2020 ERC-Consolidator Grant No. 819127, Horizon 2020 Marie Skłodowska-Curie Grant Agreement No. 700525 “NIOBE” and No. 101026516, and Horizon 2020 Marie Skłodowska-Curie RISE project JENNIFER2 Grant Agreement No. 822070 (European grants); L’Institut National de Physique Nucléaire et de Physique des Particules (IN2P3) du CNRS and L’Agence Nationale de la Recherche (ANR) under grant ANR-21-CE31-0009 (France); BMBF, DFG, HGF, MPG, and AvH Foundation (Germany); Department of Atomic Energy under Project Identification No. RTI 4002, Department of Science and Technology, and UPES SEED funding programs No. UPES/R&D-SEED-INFRA/17052023/01 and No. UPES/R&D-SOE/20062022/06 (India); Israel Science Foundation Grant No. 2476/17, U.S.-Israel Binational Science Foundation Grant No. 2016113, and Israel Ministry of Science Grant No. 3-16543; Istituto Nazionale di Fisica Nucleare and the Research Grants BELLE2; Japan Society for the Promotion of Science, Grant-in-Aid for Scientific Research Grants No. 16H03968, No. 16H03993, No. 16H06492, No. 16K05323, No. 17H01133, No. 17H05405, No. 18K03621, No. 18H03710, No. 18H05226, No. 19H00682, No. 20H05850, No. 20H05858, No. 22H00144, No. 22K14056, No. 22K21347, No. 23H05433, No. 26220706, and No. 26400255, and the Ministry of Education, Culture, Sports, Science, and Technology (MEXT) of Japan; National Research Foundation (NRF) of Korea Grants No. 2016R1D1A1B02012900, No. 2018R1A2B-3003643, No. 2018R1A6A1A06024970, No. 2019R1I1A3A01058933, No. 2021R1A6A1A-03043957, No. 2021R1F1A1060423, No. 2021R1F1A1064008, No. 2022R1A2C1003993, and No. RS-2022-00197659, Radiation Science Research Institute, Foreign Large-Size Research Facility Application Supporting project, the Global Science Experimental Data Hub Center of the Korea Institute of Science and Technology Information and KREONET/GLORIAD; Universiti Malaya RU grant, Akademi Sains Malaysia, and Ministry of Education Malaysia; Frontiers of Science Program Contracts No. FOINS-296, No. CB-221329, No. CB-236394, No. CB-254409, and No. CB-180023, and SEP-CINVESTAV Research Grant No. 237 (Mexico); the Polish Ministry of Science and Higher Education and the National Science Center; the Ministry of Science and Higher Education of the Russian Federation and the HSE University Basic Research Program, Moscow; University of Tabuk Research Grants No. S-0256-1438 and No. S-0280-1439 (Saudi Arabia); Slovenian Research Agency and Research Grants No. J1-9124 and No. P1-0135; Agencia Estatal de Investigacion, Spain Grant No. RYC2020-029875-I and Generalitat Valenciana, Spain Grant No. CIDEGENT/2018/020; The Knut and Alice Wallenberg Foundation (Sweden), Contracts No. 2021.0174 and No. 2021.0299;

National Science and Technology Council, and Ministry of Education (Taiwan); Thailand Center of Excellence in Physics; TUBITAK ULAKBIM (Turkey); National Research Foundation of Ukraine, Project No. 2020.02/0257, and Ministry of Education and Science of Ukraine; the U.S. National Science Foundation and Research Grants No. PHY-1913789 and No. PHY-2111604, and the U.S. Department of Energy and Research Awards No. DE-AC06-76RLO1830, No. DE-SC0007983, No. DE-SC0009824, No. DE-SC0009973, No. DE-SC0010007, No. DE-SC0010073, No. DE-SC0010118, No. DE-SC0010504, No. DE-SC0011784, No. DE-SC0012704, No. DE-SC0019230, No. DE-SC0021274, No. DE-SC0021616, No. DE-SC0022350, No. DE-SC0023470; and the Vietnam Academy of Science and Technology (VAST) under Grants No. NVCC.05.12/22-23 and No. DL0000.02/24-25.

These acknowledgements are not to be interpreted as an endorsement of any statement made by any of our institutes, funding agencies, governments, or their representatives.

We thank the SuperKEKB team for delivering high-luminosity collisions; the KEK cryogenics group for the efficient operation of the detector solenoid magnet; the KEK Computer Research Center for on-site computing support; the NII for SINET6 network support; and the raw-data centers hosted by BNL, DESY, GridKa, IN2P3, INFN, and the University of Victoria.

References

- [1] Belle Collaboration, *First Measurements of Absolute Branching Fractions of the Ξ_c^0 Baryon at Belle*, Phys. Rev. Lett. **122** (2019) 082001.
- [2] Belle Collaboration, *Measurements of branching fractions and asymmetry parameters of $\Xi_c^0 \rightarrow \Lambda \bar{K}^{*0}$, $\Xi_c^0 \rightarrow \Sigma^0 \bar{K}^{*0}$, and $\Xi_c^0 \rightarrow \Sigma^+ K^{*-}$ decays at Belle*, JHEP **06** (2021) 160.
- [3] Belle Collaboration, *Measurements of the branching fractions of $\Xi_c^0 \rightarrow \Lambda K_S^0$, $\Xi_c^0 \rightarrow \Sigma^0 K_S^0$, and $\Xi_c^0 \rightarrow \Sigma^+ K^-$ decays at Belle*, Phys. Rev. D **105** (2022) L011102.
- [4] Hai-Yang Cheng, *Charmed baryon physics circa 2021*, Chin. J. Phys. **78** (2022) 324-362.
- [5] J. G. Körner and M. Krämer, *Exclusive non-leptonic charm baryon decays*, Z. Phys. C **55** (1992) 659.
- [6] M. A. Ivanov, J. G. Korner, V. E. Lyubovitskij, and A. G. Rusetsky, *Exclusive nonleptonic decays of bottom and charm baryons in a relativistic three-quark model: Evaluation of nonfactorizing diagrams*, Phys. Rev. D **57** (1998) 5632.
- [7] Q. P. Xu and A. N. Kamal, *Cabibbo-favored nonleptonic decays of charmed baryons*, Phys. Rev. D **46** (1992) 270.
- [8] H. Y. Cheng and B. Tseng, *Cabibbo-allowed nonleptonic weak decays of charmed baryons*, Phys. Rev. D **48** (1993) 4188.
- [9] P. Żenczykowski, *Nonleptonic charmed-baryon decays: Symmetry properties of parity-violating amplitudes*, Phys. Rev. D **50** (1994) 5787.
- [10] J. Q. Zou, F. R. Xu, G. B. Meng, and H. Y. Cheng, *Two-body hadronic weak decays of antitriplet charmed baryons*, Phys. Rev. D **101** (2020) 014011.

- [11] K. K. Sharma and R. C. Verma, *A study of weak mesonic decays of Λ_c and Ξ_C baryons on the basis of HQET results*, Eur. Phys. J. C **7** (1999) 217.
- [12] C. Q. Geng, Y. K. Hsiao, C. W. Liu, and T. H. Tsai, *Antitriplet charmed baryon decays with $SU(3)$ flavor symmetry*, Phys. Rev. D **97** (2018) 073006.
- [13] C. Q. Geng, C. W. Liu, and T. H. Tsai, *Asymmetries of anti-triplet charmed baryon decays*, Phys. Lett. B **794** (2019) 19.
- [14] H. J. Zhao, Y. L. Wang, Y. K. Hsiao, and Y. Yu, *A Diagrammatic Analysis of Two-Body Charmed Baryon Decays with Flavor Symmetry*, JHEP **02** (2020) 165.
- [15] F. Huang, Z. P. Xing, and X. Z. He, *A global analysis of charmless two body hadronic decays for anti-triplet charmed baryons*, JHEP **03** (2022) 143.
- [16] Y. K. Hsiao, Y. L. Wang, and H. J. Zhao, *Equivalent $SU(3)_F$ approaches for two-body anti-triplet charmed baryon decays*, JHEP **09** (2022) 35.
- [17] H. Zhong, F. Xu, Q. Wen, and Y. Gu, *Weak decays of antitriplet charmed baryons from the perspective of flavor symmetry*, JHEP **02** (2023) 235.
- [18] Z. P. Xing, *et al.*, *Global analysis of measured and unmeasured hadronic two-body weak decays of antitriplet charmed baryons*, Phys. Rev. D **108** (2023) 053004.
- [19] C. Q. Geng, *et al.*, *Complete determination of $SU(3)_F$ amplitudes and strong phase in $\Lambda_c^+ \rightarrow \Xi^0 K^+$* , Phys. Rev. D **109** (2024) L071302.
- [20] H. Zhong, F. Xu, and H. Y. Cheng *Analysis of Hadronic Weak Decays of Charmed Baryons in the Topological Diagrammatic Approach*, arXiv:2404.01350.
- [21] CLEO Collaboration, *Measurement of the decay asymmetry parameters in $\Xi_c^0 \rightarrow \Xi^- \pi^+$* , Phys. Rev. D **63** (2001) 111102.
- [22] Belle Collaboration, *Measurements of the Branching Fractions of the Semileptonic Decays $\Xi_c^0 \rightarrow \Xi^- \ell^+ \nu_\ell$ and the Asymmetry Parameter of $\Xi_c^0 \rightarrow \Xi^- \pi^+$* , Phys. Rev. Lett. **127** (2021) 121803.
- [23] Belle Collaboration, *The Belle detector*, Nucl. Instr. and Methods Phys. Res. Sect. A **479** (2002) 117.
- [24] Belle Collaboration, *Physics achievements from the Belle experiment*, Prog. Theor. Exp. Phys. **2012** (2012) 04D001.
- [25] S. Kurokawa and E. Kikutani, *Overview of the KEKB accelerators*, Nucl. Instr. and Methods Phys. Res. Sect. A **499** (2003) 1, and other papers included in this volume.
- [26] T. Abe *et al.*, *Achievements of KEKB*, Prog. Theor. Exp. Phys. **2013** (2013) 03A001, and references therein.
- [27] Belle II Collaboration, *Belle II Technical Design Report*, arXiv:1011.0352.
- [28] SuperKEKB Collaboration, *SuperKEKB Collider*, Nucl. Instr. and Methods Phys. Res. Sect. A **907** (2018) 188.
- [29] T. Sjöstrand *et al.*, *High-energy physics event generation with PYTHIA 6.1*, Comput. Phys. Commun. **135** (2001) 238.
- [30] T. Sjöstrand *et al.*, *An introduction to PYTHIA 8.2*, Comput. Phys. Commun. **191** (2015) 159.

- [31] D.J. Lange, *The EvtGen particle decay simulation package*, Nucl. Instr. and Methods Phys. Res. Sect. A **462** (2001) 152.
- [32] S. Jadach, B. F. L. Ward and Z. Wąs, *The precision Monte Carlo event generator KK for two-fermion final states in e^+e^- collisions*, Comput. Phys. Commun. **130** (2000) 260.
- [33] E. Barberio and Z. Wąs, *PHOTOS: A Universal Monte Carlo for QED radiative corrections. Version 2.0*, Comput. Phys. Commun. **79** (1994) 291.
- [34] R. Brun *et al.*, *GEANT3*, CERN Report No. DD/EE/84-1 (1984).
- [35] GEANT4 collaboration, *GEANT4—a simulation toolkit*, Nucl. Instrum. Methods Phys. Sect. A **506** (2003) 250.
- [36] Belle II Framework Software Group, *The Belle II Core Software*, Comput. Softw. Big Sci. **3** (2019) 1.
- [37] M. Gelb *et al.*, *B2BII: Data Conversion from Belle to Belle II*, Comput. Softw. Big Sci. **2** (2018) 9.
- [38] J.-F. Krohn *et al.*, *Global decay chain vertex fitting at Belle II*, Nucl. Instrum. Methods Phys. Res., Sect. A **976** (2020) 164269.
- [39] E. Nakano, *Belle PID*, Nucl. Instrum. Methods Phys. Res., Sect. A **494** (2002) 402.
- [40] Belle Collaboration, *Observation of an Excited Ω^- Baryon*, Phys. Rev. Lett. **121** (2018) 052003.
- [41] Belle Collaboration, *Measurement of the resonant and nonresonant branching ratios in $\Xi_c^0 \rightarrow \Xi^0 K^+ K^-$* , Phys. Rev. D **103** (2021) 112002.
- [42] Belle Collaboration, *Search for the semileptonic decays $\Xi_c^0 \rightarrow \Xi^0 \ell^+ \ell^-$ at Belle*, Phys. Rev. D **109** (2024) 052003.
- [43] Particle Data Group, *The Review of Particle Physics*, Phys. Rev. D **110**, 030001 (2024).
- [44] G. Punzi, *Sensitivity of searches for new signals and its optimization*, eConf **C030908** (2003) MODT002. arXiv:physics/0308063.
- [45] J. E. Gaiser, *Charmonium Spectroscopy From Radiative Decays of the J/ψ and ψ'* , Ph. D. thesis, Stanford Linear Accelerator Center, Stanford University, Report No. SLAC-R-255, 1982.
- [46] X. Y. Zhou, S. X. Du, G. Li, and C. P. Shen, *TopoAna: A generic tool for the event type analysis of inclusive Monte-Carlo samples in high energy physics experiments*, Comput. Phys. Commun. **258** (2021) 107540.
- [47] K. S. Cranmer, *Kernel estimation in high-energy physics*, Comput. Phys. Commun. **136** (2001) 198.
- [48] G. D’Agostini, *On the use of the covariance matrix to fit correlated data*, Nucl. Instrum. Methods Phys. Res., Sect. A **346** (1994) 306.
- [49] I. Antcheva *et al.*, *ROOT — A C++ framework for petabyte data storage, statistical analysis and visualization*, Comput. Phys. Commun. **180** (2009) 2499.

A $M(\Xi^0\pi^0)$ spectra in $\cos\theta_{\Xi^0}$ bins

Distributions of $M(\Xi^0\pi^0)$ in bins of $\cos\theta_{\Xi^0}$ are shown in figure 6 with fit results overlaid.

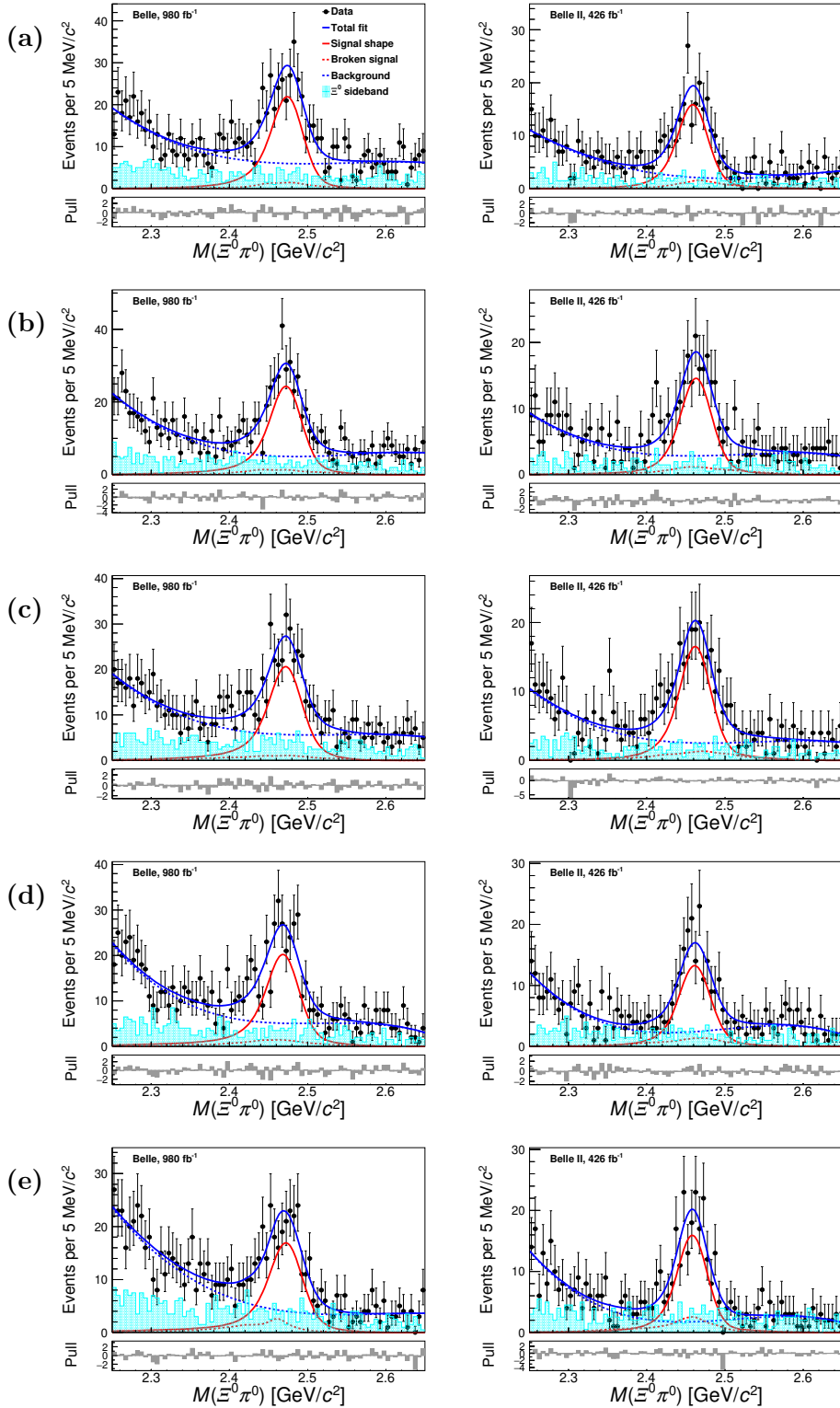


Figure 6. Invariant mass distributions of $\Xi_c^0 \rightarrow \Xi^0 \pi^0$ candidates from (left) Belle and (right) Belle II data samples in $\cos\theta_{\Xi^0}$ bins of (a) $(-1.0, -0.6)$, (b) $(-0.6, -0.2)$, (c) $(-0.2, 0.2)$, (d) $(0.2, 0.6)$ and (e) $(0.6, 1.0)$. The markers with error bars represent the data. The solid blue curves, solid red curves, dashed red curves, and dashed blue curves show the total fit, signal shape, broken-signal shape, and smooth backgrounds, respectively. The cyan histograms show the data from the Ξ^0 mass sidebands.